AD_____

Award Number: W81XWH-09-1-0405

TITLE: Understanding collagen organization in breast tumors to predict and prevent metastasis

PRINCIPAL INVESTIGATOR:Edward Brown

CONTRACTING ORGANIZATION:
University of Rochester Medical Center
Rochester, NY 14642

REPORT DATE: September 2010

TYPE OF REPORT: Annual

PREPARED FOR: U.S. Army Medical Research and Materiel Command
               Fort Detrick, Maryland 21702-5012

DISTRIBUTION STATEMENT:

    √ Approved for public release; distribution unlimited

The views, opinions and/or findings contained in this report are
those of the author(s) and should not be construed as an official
Department of the Army position, policy or decision unless so
designated by other documentation.

REPORT DOCUMENTATION PAGE

Form Approved
OMB No. 0704-0188

Public reporting burden for this collection of information is estimated to average 1 hour per response, including the time for reviewing instructions, searching existing data sources, gathering and maintaining the data needed, and completing and reviewing this collection of information. Send comments regarding this burden estimate or any other aspect of this collection of information, including suggestions for reducing this burden to Department of Defense, Washington Headquarters Services, Directorate for Information Operations and Reports (0704-0188), 1215 Jefferson Davis Highway, Suite 1204, Arlington, VA 22202-4302. Respondents should be aware that notwithstanding any other provision of law, no person shall be subject to any penalty for failing to comply with a collection of information if it does not display a currently valid OMB control number. **PLEASE DO NOT RETURN YOUR FORM TO THE ABOVE ADDRESS.**

1. REPORT DATE (DD-MM-YYYY)	2. REPORT TYPE	3. DATES COVERED (From - To)
01-09-2010	Annual	1 SEP 2009 – 31 AUG 2010

4. TITLE AND SUBTITLE
Understanding collagen organization in breast tumors to predict and prevent metastasis

5a. CONTRACT NUMBER

5b. GRANT NUMBER
W81XWH-09-1-0405

5c. PROGRAM ELEMENT NUMBER

6. AUTHOR(S)
Edward Brown

go ckn²"gf y ctf adtqy pB wo e0qej guvgt0gf w

5d. PROJECT NUMBER

5e. TASK NUMBER

5f. WORK UNIT NUMBER

7. PERFORMING ORGANIZATION NAME(S) AND ADDRESS(ES)

University of Rochester Medical Center

Rochester, NY 14642

8. PERFORMING ORGANIZATION REPORT NUMBER

9. SPONSORING / MONITORING AGENCY NAME(S) AND ADDRESS(ES)
U.S. Army Medical Research and Materiel Command
Fort Detrick, MD 21702-5012

10. SPONSOR/MONITOR'S ACRONYM(S)

11. SPONSOR/MONITOR'S REPORT NUMBER(S)

12. DISTRIBUTION / AVAILABILITY STATEMENT
Approved for public release; distribution unlimited

13. SUPPLEMENTARY NOTES

14. ABSTRACT
The ordering of collagen fibers within a tumor has significant influence on tumor metastasis: in murine breast tumor models, tumor cells move towards blood vessels along fibers that are visible via second harmonic generation (SHG), and SHG is exquisitely sensitive to molecular ordering. Tumor cells that are moving along SHG-producing (i.e. ordered) collagen fibers move significantly faster than those cells that are moving independently of SHG-producing fibers, and the extent of SHG-associated tumor cell motility is correlated with metastatic ability of the tumor model. Furthermore, the tumor-host interface of murine breast tumor models is characterized by radially oriented SHG-producing fibers associated with tumor cells invading the surrounding tissue. Consequently we believe that the process of establishing ordered fibers offers an exciting, and currently unexploited, therapeutic target. To take advantage of this, we must first learn the cellular players and molecular signals by which collagen ordering is induced. Therefore, in this application we propose to determine the key cells and signals which influence the ordering of collagen in breast tumors, determine if this ordering is predictive of metastasis, and develop new optical tools to study this ordering.

15. SUBJECT TERMS
Microscopy, metastasis

16. SECURITY CLASSIFICATION OF:

a. REPORT	b. ABSTRACT	c. THIS PAGE	17. LIMITATION OF ABSTRACT	18. NUMBER OF PAGES	19a. NAME OF RESPONSIBLE PERSON USAMRMC
U	U	U	UU	39	19b. TELEPHONE NUMBER (include area code)

Standard Form 298 (Rev. 8-98)
Prescribed by ANSI Std. Z39.18

Table of Contents

Introduction.

The extent and nature of the ordering of collagen fibers within a tumor has significant influence on the process of tumor metastasis: in murine breast tumor models, tumor cells move towards blood vessels along fibers that are visible via second harmonic generation (SHG), and SHG is exquisitely sensitive to molecular ordering (see below). Tumor cells that are moving along SHG-producing (i.e. ordered) collagen fibers move significantly faster than those cells that are moving independently of SHG-producing fibers, and the extent of SHG-associated tumor cell motility is correlated with metastatic ability of the tumor model. Furthermore, the tumor-host interface of murine breast tumor models is characterized by radially oriented SHG-producing fibers associated with tumor cells invading the surrounding tissue. Lastly, we have shown that treatment of tumors with the hormone relaxin, known to alter metastatic ability, alters the collagen ordering as detectable by SHG.

As locomotion along ordered (SHG-producing) fibers plays a pivotal role in the metastatic process, we believe that the process of establishing ordered fibers offers an exciting, and currently unexploited, therapeutic target. To take advantage of this, we must first learn the cellular players and molecular signals by which collagen ordering is induced. Therefore, in this application we propose to *determine the key cells and signals which influence the ordering of collagen in breast tumors*. We will do this by disrupting candidate cells and signals in mouse models of breast cancer using SHG-based measures of collagen ordering, and metastasis, as readouts. Additionally, we will *determine if SHG measures of collagen ordering in breast tumors are clinically useful predictors of metastatic outcome in breast cancer patient biopsies*.

This work will have great impact for several reasons. It will provide important insight into the molecular and cellular mechanisms by which the collagen in breast tumors is ordered, and how this ordering affects metastatic ability. In future work we can then exploit these findings by developing and evaluating clinically useful therapeutic techniques that will target, for the first time, the ordering of tumor collagen and hence attempt to inhibit metastatic ability, improving patient survival. This project will also explore whether collagen ordering in the tumor, as quantified by SHG, is a clinically viable predictor of metastatic outcome in patient biopsies. A measure of metastatic ability is extremely exciting, because there is currently an identified, pressing need for patient stratification based upon metastatic risk, in order to minimize 'over treatment' of patients who only require local therapy after resection, not systemic chemotherapy[6]. This would improve patients' quality of life. Hence, this project has promise to be clinically relevant through two separate paths.

Body

The Statement of Work for this grant proposal is as follows:

Statement of Work

Specific Aim 1. Determine the role of macrophages in governing collagen ordering in tumors, and their mechanism of action. (Months 1-30)

1a) Modulate the presence of macrophages, then evaluate the effects on collagen ordering in tumors, and the effects on metastatic burden. (Months 1-12) Uses liposome treatment. ~50 mice. Verifies involvement of macrophages' in collagen ordering in tumors, the exact nature of their particular impact on collagen ordering, and the impact on metastasis.

1b) Manipulate the expression of candidate genes in macrophages, and evaluate the effects on collagen ordering in tumors, and the effects on metastatic burden (Months 13-30) Uses bone marrow transfer after irradiation. Source animals are one of 7 knockouts, for 7 candidate genes. ~50x7= 350 mice. Produces identity of key signaling molecules involved in collagen ordering in tumors, the exact nature of their particular impact on collagen ordering, and the impact on metastasis.

Specific Aim 2. Determine the role of Th1, Th2, and Tregs in governing collagen ordering in tumors, and their mechanism of action. (Months 31-60)

2a) Modulate the presence of each cell type, then evaluate the effects on collagen ordering in tumors, and the effects on metastatic burden.(Months 31-42) Uses cell transfer after antibody treatment. ~3x50=150 mice. Produces identity of key cells involved in collagen ordering in tumors, the exact nature of their particular impact on collagen ordering, and the impact on metastasis.

2b) Manipulate the expression of candidate genes in those cell types found significant in 2a, and evaluate the effects on collagen ordering in tumors, and the effects on metastatic burden (Months 43-60) Uses cell transfer after antibody treatment. Source animals are one of 7 knockouts, for 7 candidate genes. ~3x50x7=1050 mice. Produces identity of key signaling molecules involved in collagen ordering in tumors, the exact nature of their particular impact on collagen ordering, and the impact on metastasis.

Specific Aim 3. Determine if collagen ordering is a clinically useful predictor of metastatic ability in human tissue samples (Months 1-60).

1a) In archival specimens from breast tumors we will evaluate the predictive relationships between collagen ordering and metastatic outcome (Months 1-60). Uses pathology samples of 4 breast tumor types to determine if SHG can predict metastatic outcome. ~4x50=200 samples. Produces an assessment of SHG's predictive ability.

We have concentrated on developing, proving, and utilizing the molecular tools required to manipulate macrophage populations in the E0771 tumor model in order to advance the goals of Specific Aim 1, while also establishing the staining and quantification regimen required to determine an optical "order index" or OI, which is required to advance the goals of all three specific aims.

A crucial point to prove early in experimentation is that only mature, phagocytic peripheral macrophages are affected by administration of intraorbital clodronate liposomes. Although significant literature exists to indicate that macrophages are heavily affected by application of both the free ion and the liposome, potential effects on other marrow-derived cell types have been left largely unstudied. As all cells are capable of phagocytosis to some extent, liposome intake by non-macrophage cells could be problematic. Most importantly to this project, potential effects on the marrow-derived fibroblast population have not been determined to date. As we believe that fibroblasts are the cells which directly manipulate collagen structure in response to various signals from macrophages, the possibility that marrow-derived fibroblasts (anywhere from 7-29% of total fibroblast populations in various types of solid carcinoma) would be affected is too great to ignore. Therefore, a series of *in vitro* experiments were performed to determine whether fibroblasts responding to various stimuli present in tumors would be affected by clodronate administration.

To this end, HFF-1 human foreskin fibroblasts were treated by exposure to cell culture media containing one of the following groups:

1. Control (4.5 g/L glucose, 10% FCS, 1% Penicillin/streptomycin)
2. Simulated bacterial/viral infection response (LPS/IFN-γ) [2]
3. High M2 macrophage activity (IL-4) [2]
4. Induction of phagocytosis, suppression of Th1 activity and autoimmunity (IL-10) [3]
5. Transition to activated/myofibroblast phenotype (TGF-β1, doses) [4]
6. Highly inflamed/wound response environment (TNF-α, doses) [5]
7. Tumor-conditioned media (supernatants of Tg1-1 adenocarcinoma culture)

Briefly, HFF-1 fibroblasts were seeded at 5×10^4/well in a 96-well plate and exposed to culture conditions as desired for 48hr. For Experiment 1, cells were then exposed to 2um red fluorescent carboxylate-modified fluorescent styrene beads for 4hr to induce phagocytosis, then exposed for 30min to fluo-4 calcium indicator dye. Excess beads were washed off and fluorescence levels of both red beads and fluo-4 were determined via plate reader. The idea was to get a measure of the extent of phagocytosis (red beads) versus the total number of cells present (fluo-4) in response to environmental stimuli. For this experiment, RAW264.7 murine macrophages were included to ascertain that the treatments were working (by making use of characteristic changes in macrophage morphology in response to these stimuli). See Figure 1 for results. In summary, this experiment revealed that fibroblasts will readily phagocytose in conditions representative of the tumor environment (thereby taking up liposomes intended for macrophage depletion), although at a significantly lower rate than macrophages. Consequently, the effect of this phagocytosis on these fibroblasts has to be quantified. This was evaluated by culturing and treating fibroblasts as before, then incubating them with a DNA-binding dye to ascertain proliferation. See Figure 2 for results. In summary, this experiment revealed that while the fibroblasts phagocytose liposomes to a limited extent under culture conditions representative of the tumor microenvironment, their proliferation is not affected. These two pilot experiments, taken together, indicate that the use of clodronate

liposomes is unlikely to affect fibroblasts in the stroma or cause a confound in terms of measuring collagen organization *in vivo*.
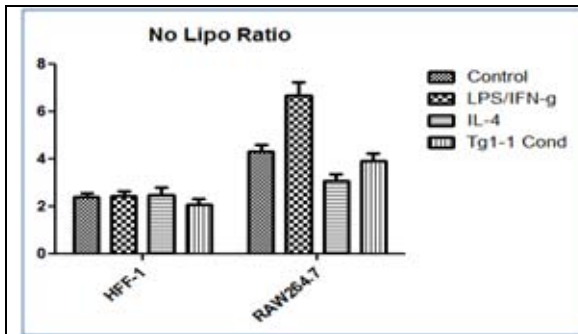

Figure 1: The effects of a subset of culture conditions on phagocytosis relative to cell number, here termed 'phagocytic index', in HFF-1 and RAW264.7 cells. Fibroblasts exposed to the classical macrophage activators LPS/IFN-γ and the alternative macrophage activator IL-4 show no alteration in phagocytosis relative to cell number, whereas a possible slight decrease in phagocytic activity is noticed when the fibroblasts are exposed to tumor-conditioned media (n=48 wells all groups). This is in contrast to results seen in RAW264.7 macrophages, where LPS/IFN-γ elevates phagocytic activity while curtailing proliferation (high phagocytic index) and IL-4 does the converse – both of which are expected outcomes based upon macrophage studies. Interestingly, tumor-conditioned media also failed to impact macrophage phagocytic activity relative to control.
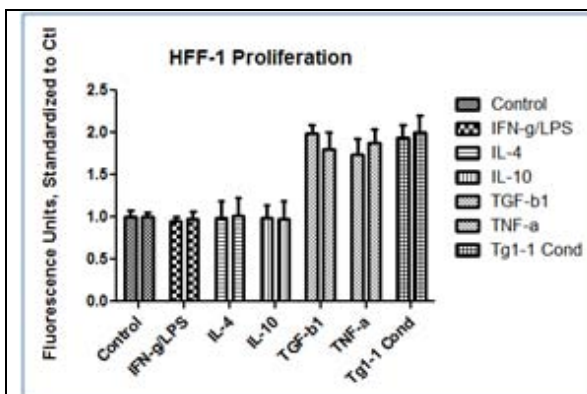

Figure 2: The proliferation of fibroblasts in culture in response to a complete set of culture conditions when exposed to PBS-containing control liposomes (left bars in each pair) and clodronate-containing liposomes (right bars). In no culture condition did clodronate liposomes significantly affect fibroblast proliferation and survival as quantified by DNA-binding CyQuant proliferation assay. Although certain signals increased fibroblast proliferation as expected, there was no additional effect of liposome treatment on the population (p=.5452, n= 16 each group).

To determine if the clodronate liposomes affected our tumor cells, we tested the effects of administration of clodronate liposome on the murine breast adenocarcinoma E0771 and compared them to the effects on HFF-1 fibroblasts and RAW264.7 macrophages.See Figure 3 for results. In summary, there was no effects on E0771 tumor cells nor again on cultured fibroblasts, while RAW264.7 macrophages were significantly depleted.
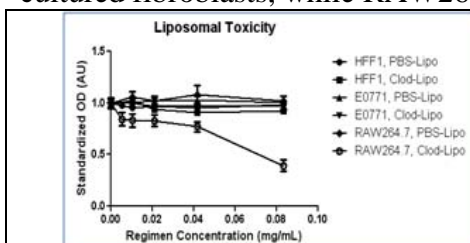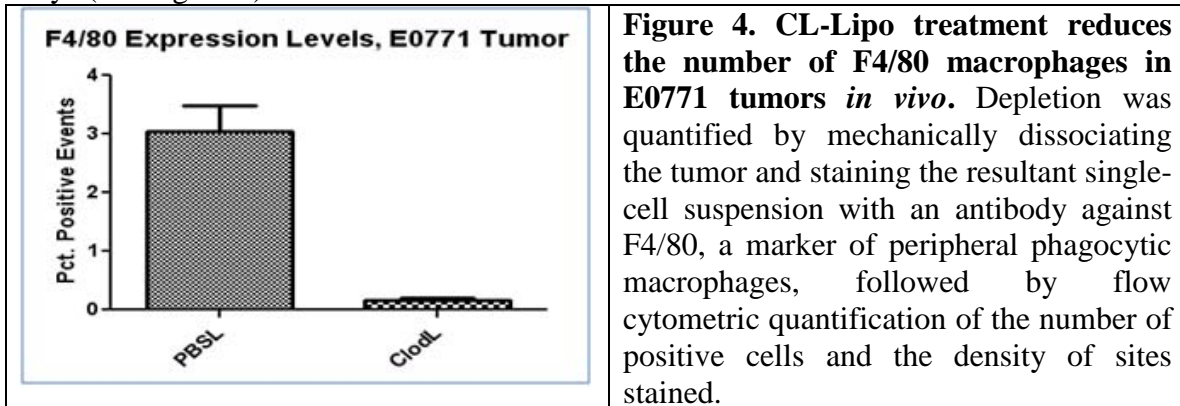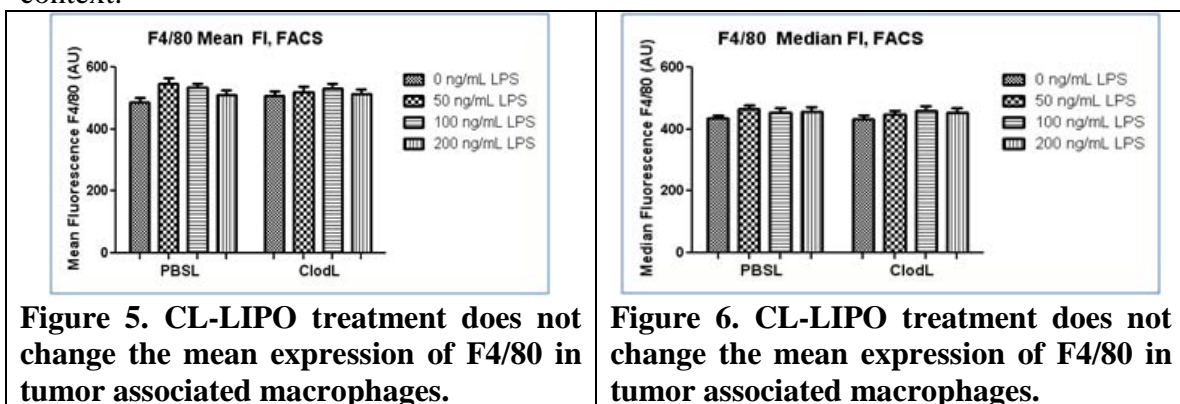

Figure 3: Effect of clodronate liposomes on E0771 tumor cells. Although clodronate acts in a dose-dependent manner to kill RAW264.7 macrophages, there is no toxic effect on E0771 adenocarcinoma or HFF-1 fibroblasts.

The next required task was to titrate the amount of clodronate required to completely deplete peripheral macrophages without causing damage to the animal model. Clodronate liposome administration at a dose indicated by two studies caused extensive damage to liver lobes in the form of fibrosis, scarring, and fatty degeneration. Upon titration of the reagent, it was found that .1cc injected every 3 days at a dilution of 1:3 in PBS was sufficient to cause nearly complete macrophage depletion in the tumor at 21 days (see Figure 4).

Figure 4. CL-Lipo treatment reduces the number of F4/80 macrophages in E0771 tumors *in vivo*. Depletion was quantified by mechanically dissociating the tumor and staining the resultant single-cell suspension with an antibody against F4/80, a marker of peripheral phagocytic macrophages, followed by flow cytometric quantification of the number of positive cells and the density of sites stained.

Although the number of positive events (cells expressing F4/80) decreases as a result of clodronate administration, the density of F4/80 expression (the mean and median fluorescence intensity of each positive cell) is unaffected in macrophages (Figures 5 and 6). This indicates that clodronate administration truly depletes the number of F4/80 macrophages within E0771 tumors, and does not simply reduce F4/80 expression in the macrophages. Further markers have also been studied for use – literature indicates that some TAMs express either MOMA-1 or CD11b in addition to or instead of F4/80, and these markers are also being stained for as a regular procedure. Thus far, depletion has affected all of these cohorts of the TAM population to a fairly equal extent (data not shown), indicating that clodronate depletion is an acceptable technique to use in this context.

Figure 5. CL-LIPO treatment does not change the mean expression of F4/80 in tumor associated macrophages.

Figure 6. CL-LIPO treatment does not change the mean expression of F4/80 in tumor associated macrophages.

Now that clodronate liposomes have been established as a usable and reproducible method in our laboratory for the depletion of macrophages in mouse models of cancer, the effects of this depletion on the ordering of collagen I in the tumor can be studied. The first such experiment is to implant E0771 mammary adenocarcinoma in the female mouse mammary fat pad. This cell line is aggressive and metastatic, making it a good candidate for growth studies. The expectation is that tumors will show impediments to collagen organization as determined by SHG imaging when macrophages are absent relative to control mice. This effect is expected to be strong in breast tumors located in breast tissue.

In Figure 9 we report two separate full experiments in which this procedure was done. Briefly, mice were anesthetized and implanted with E0771 subcutaneously in the mammary fat pad, then administered a dose of the appropriate liposome via retroocular injection. Every third day subsequent, mice were anesthetized and the retroocular injection was performed in the opposing orbit to minimize possible damage. On day 21, mice were sacrificed and the tumors were removed, sectioned, and stained for markers of interest. All sections analyzed were mounted on a single large slide to ensure that immunofluorescence levels were as comparable as possible. Sample preparation was followed by two-photon imaging, in which simultaneous capture of SHG and immunofluorescence of collagen I (IF) was accomplished (amongst other markers). Both experiments (n=8 and 7, n=10 and 10) indicate at the very least a trend toward decrease in the ratio of SHG to IF (defined as the ordering index or OI) in response to clodronate TAM ablation, as posited by our group, and while the run shown in Figure 9 was statistically significant (p<0.05) the run shown in Figure 10 had greatly increased noise and hence was not. This result is therefore very exciting to us, and further runs are currently being performed to complete this experiment and quantitatively determine the decrease in OI due to absence of TAMs.
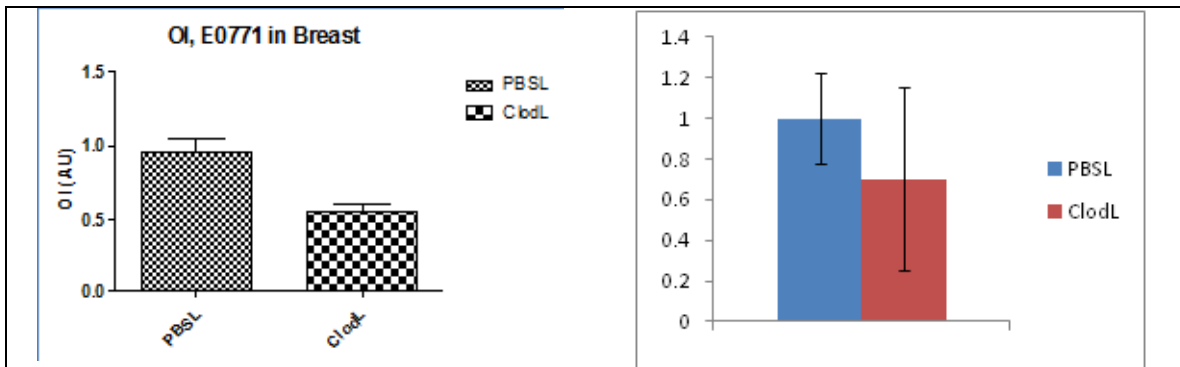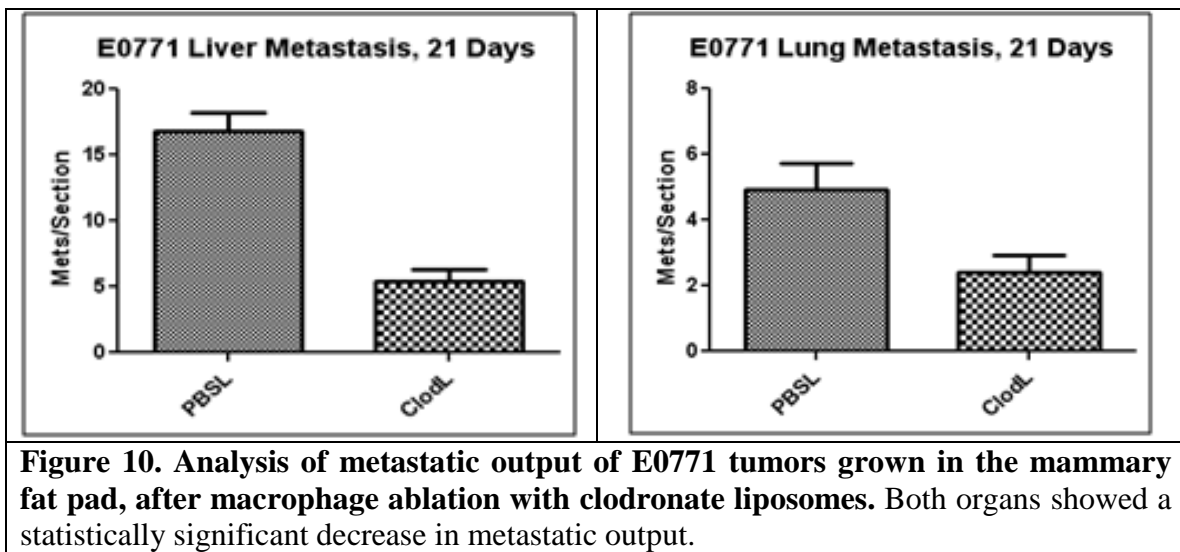

Figure 9. Two experimental measurements of the change in OI (ordering index) upon depletion of F4/80 macrophages. Depletion of macrophages was confirmed by separate FACS analysis. The depletion in the first experimental run (left) was statistically significant (p<0.05) while the second was not.
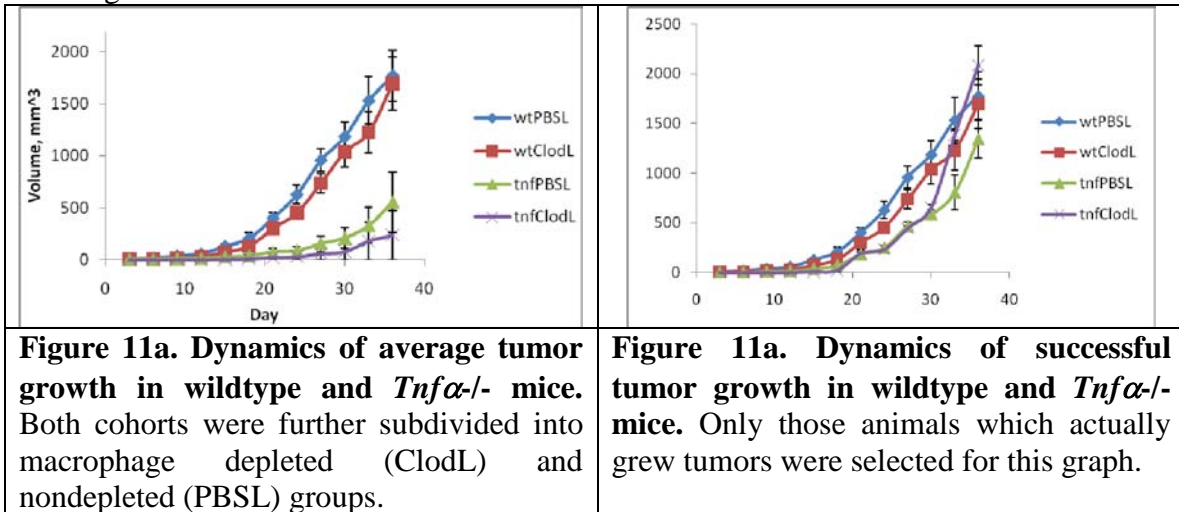
Due to literature implicating certain gene products of macrophages in the establishment of distant metastasis in various malignancies, metastatic burden in the liver and lungs was quantified by a surgical pathologist in hematoxylin/eosin-stained sections. Criteria for determining a metastasized cancer cell from surrounding normal tissue involve (in part): ratio of nucleus to cytoplasm, appearance of nucleus, size, overall cell morphology, and presence or absence of abnormal mitotic structures. When sections from lungs and liver from the orthotopic E0771 cohort shown in Figure 9a were analyzed in this manner, it was discovered that clodronate-induced macrophage depletion significantly decreases the metastatic burden in both organs. Figure 10 shows this effect. To further examine this effect, both E0771 and MCA38 cell lines are in the process of being stably transfected with eGFP to streamline metastasis quantification in the future.

Figure 10. Analysis of metastatic output of E0771 tumors grown in the mammary fat pad, after macrophage ablation with clodronate liposomes. Both organs showed a statistically significant decrease in metastatic output.

Also of interest is the molecular mechanism by which tumor-associated macrophages are able to conduct these alterations in collagen ordering in breast and colorectal tumors. To this end, a number of candidate genes are to be evaluated during the course of this project. The candidate genes currently being evaluated are: *Tnfα, Tgfβl, Egf, Il10,* and *Ifnγ.* Knockout mice deficient in these gene products have been purchased from various commercial vendors, and breeding colonies started. Of these gene products, only *Tgfβl* deficiency is homozygous lethal, and therefore all mice studied for this gene will be heterozygotes.

As we are interested eventually in creating chimeric animals that carry myeloid-derived cells (i.e. macrophages) deficient in desired gene products via adoptive transfer of bone marrow into wildtype animals, and this experimental procedure is exhaustive of both time and animal number, we therefore are performing a preliminary experiment in which E0771 breast tumors were grown in each strain of knockout mouse, then compared these data to data derived from wildtype mice in a preliminary attempt to determine possible gene knockout effects. This set of experiments is currently ongoing in the lab with all strains save *Egf-/-*, which is still being rederived from commercial stocks.

The first strain to undergo such experimentation is *Tnfα-/-*. Mice were separated into two groups (PBSL and ClodL, n=9 each) as previously, and were compared to a new wildtype cohort also separated into two groups (PBSL and ClodL, n=10 and 9). Tumors were measured with Vernier calipers every three days on the long and short axis, then volume was calculated assuming the tumor shape as a prolate spheroid. This approximation holds up well until the more advanced time points, when it is possible that volume is slightly underestimated due to invasion into the body wall. At the end of the experimental timecourse, tumors, lungs, and livers were resected, prepared, and analyzed as already described. As Figure 11 shows, the average tumor volume increased with significantly slower dynamics in the two subgroups of the *Tnfα-/-* cohort, although the error bars were quite large in both subgroups (Figure 11a). This was because in each subgroup, 7 of 9 animals produced no detectable tumors, while 2 of 9 produced tumors which grew in a similar fashion to the 9 tumors in the wildtype cohorts (Figure 11b), although we reconfirmed the genotype in each animal a second time. All wildtype mice developed tumors, and clodronate injection only slightly impaired tumorigenesis in both wildtype and knockout animals. Figure 11b includes only those mice that developed tumors to clarify the growth courses. From these curves, we see that in animals that develop tumors, there is a slight delay in tumorigenesis in wildtype versus *Tnfα-/-* mice, and that within each strain, liposome species has little or no effect on malignant progression in terms of total tumor volume. This experiment is currently being repeated in the lab with this and other knockout strains to further elucidate differences in tumorigenesis.

Figure 11a. Dynamics of average tumor growth in wildtype and *Tnfα-/-* mice. Both cohorts were further subdivided into macrophage depleted (ClodL) and nondepleted (PBSL) groups.	Figure 11a. Dynamics of successful tumor growth in wildtype and *Tnfα-/-* mice. Only those animals which actually grew tumors were selected for this graph.

As part of this work we are also undertaking to add to our arsenal of optical tools which we use to study the tumor extracellular matrix. One of these tools is Multiphoton Fluorescence Recovery After Photobleaching (MPFRAP), which can measure the diffusion coefficient of fluorescent tracers with three-dimensional resolution. Using this tool to study the diffusive properties of fluorescent tracers after manipulating cells and signals as described above will provide powerful insight into how those cells are defining the tumor ECM. However, MPFRAP as it is currently formulated from my original invention of the technique (Brown et al Biophys J 1999) does not account for the presence of nearby barriers to diffusion, such as the omnipresent cell walls of nearby

cells. Hence it is currently entirely unsuited for accurate measurement of diffusion coefficients *in vivo*. We have fixed this, and as it is explained fully in a manuscript submitted for publication, I will append that manuscript to this report and summarize here: we performed a series of Monte Carlo simulations of MPFRAP experiments and determined the range of safe distances at which adjacent barriers of various geometries will not affect the accuracy of reported diffusion coefficients. We also derived and tested new fitting models for MPFRAP which allow accurate diffusion coefficients to be produced even when the barriers to diffusion are significantly closer than previously allowed.

Key Research Accomplishments in the first year:
Fully tested the ability of clodronate liposomes to selectively ablate macrophages *in vitro*, and evaluated their specificity for that cell type.

Used clodronate liposomes to ablate tumor associated macrophages in vivo, verified ablation, and found that this ablation affected the collagen ordering index (OI) as well as metastatic output.

Began preliminary experiments using knockout animals, determining that ablation of TNFa from all host cells (not just macrophages) caused a significant growth delay, and that manipulation of the macrophage population does not affect this growth delay.

Enabled MPFRAP to be performed in the vicinity of barriers to diffusion such as nearby cell walls, thereby allowing its use in the crowded *in vivo* environment.

Reportable Outcomes:
Over the last year I have submitted one manuscript based upon work funded in part by this award:
Sullivan K, Brown E (2010) Diffusion and multi-photon fluorescence recovery after photobleaching in bounded systems Manuscript Submitted

I have also been invited to produce one book chapter:
Han X, Perry S, Brown E Second Harmonic Imaging of Tumors. In: Campagnola P, Pavone F (eds). Second Harmonic Generation Imaging. Taylor and Francis Press. *In Preparation.*

I have also given four invited talks:
"Studying the tumor extracellular matrix using nonlinear microscopy" Invited lecture presented at the Imaging Science & Technology Rochester Chapter Meeting, Rochester, NY, 2010

"Studying cellular and molecular transport in tumors using multiphoton laser-scanning microscopy" Invited lecture presented at the University of Virginia, 2010

"Diffusion and multi-photon fluorescence recovery after photobleaching in bounded systems" Invited lecture presented at the Carl Ludwig Institute of Physiology, University of Leipzig, Leipzig, Germany, 2010

"Studying cellular and molecular transport in tumors using multiphoton laser-scanning microscopy" Invited lecture presented at Cornell University, 2010

Conclusion
In conclusion, I believe that I have made significant progress on the goals outlined in my Era of Hope Scholar Research Award.

Multiphoton Fluorescence Recovery After Photobleaching in Bounded Systems

Kelley D. Sullivan

Department of Physics and Astronomy,

University of Rochester, Rochester NY 14627

Edward B. Brown

Department of Biomedical Engineering,

University of Rochester, Rochester NY 14627*

(Dated: September 28, 2010)

Abstract

Multi-photon fluorescence recovery after photobleaching (MP-FRAP) is a laser microscopy technique used to measure diffusion coefficients of macromolecules in biological systems. The three-dimensional resolution and superior depth penetration within scattering samples offered by MP-FRAP make it an important tool for investigating both *in vitro* and *in vivo* systems. However, biological systems frequently confine diffusion within solid barriers, and to date the effect of such barriers on the measurement of absolute diffusion coefficients via MP-FRAP has not been studied. We have used Monte Carlo simulations of diffusion and MP-FRAP to understand the effect of barriers of varying geometries and positions relative to the two-photon focal volume. Furthermore, we supply ranges of barrier positions within which MP-FRAP can confidently be employed to measure accurate diffusion coefficients. Finally, we produce two new MP-FRAP models that can produce accurate diffusion coefficients in the presence of a single or parallel infinite plane boundaries positioned parallel to the optical axis, up to the resolution limit of the multi-photon laser scanning microscope.

---

* Edward_Brown@urmc.rochester.edu

I. INTRODUCTION

Multiphoton fluorescence recovery after photobleaching (MP-FRAP) is a laser microscopy technique typically employed to measure diffusion coefficients within biological systems. MP-FRAP is performed by using a brief, high-intensity, laser flash to generate photobleaching within a region of interest in a fluorescent sample. The laser is then attenuated and the region of interest is monitored as still-fluorescent molecules from outside the region diffuse in to replace the outwardly diffusing bleached molecules. The resulting fluorescence *versus* time curve can be fitted to simple analytical formulae to produce the diffusion coefficient of the mobile fluorophore. In an MP-FRAP experiment, fluorescence and photobleaching are both generated via multiphoton excitation [1]. The intrinsic spatial confinement of multiphoton excitation results in a three-dimensionally resolved bleaching/monitoring volume [2], and allows MP-FRAP to measure three-dimensionally resolved diffusion coefficients within intact samples. This intrinsic spatial confinement obviates the need for a confocal pinhole and allows MP-FRAP, as well as the multiphoton laser-scanning microscope upon which it is based, to probe living tissue down to depths of several hundred microns.

Other techniques employed to measure biological diffusion include fluorescence recovery after photobleaching (FRAP), FRAP with spatial Fourier analysis (SFA-FRAP), and fluorescence correlation spectroscopy (FCS). FRAP is the precursor to MP-FRAP and was developed in the 1970's [3–5] to probe transport parameters in biological systems. However, due to the lack of spatial confinement of the one-photon excitation process, FRAP is limited to thin samples ($< 1~\mu m$) such as the plasma membrane of a cell. The use of spatial Fourier analysis allows SFA-FRAP [6] to probe diffusion in intact thick tissue, but the technique has low spatial resolution ($\sim 40~\mu m$) and is limited to the depth penetration of epifluorescence microscopy ($\sim 50~\mu m$). FCS comes in both one-photon [7, 8] and two-photon [9, 10] varieties and like MP-FRAP it can be used to measure diffusion with high, three-dimensional, resolution. FCS relies on low fluorophore concentrations (with accompanying low signals) to produce large population fluctuations within the focal volume, while FRAP relies on high fluorophore concentrations (with accompanying large signals), making the two techniques complementary, especially in the difficult optical environment of scattering tissue.

MP-FRAP has been employed to measure absolute diffusion coefficients in the cytoplasm of cells [1, 11], cartilage [12], optically fabricated gels [13], and blood plasma [14]. In these

cases, the volume surrounding the bleached spot was assumed to be "open," with barriers to diffusion at infinity. However, many biological systems inherently confine measurements to regions within solid barriers to diffusion, such as cell walls and organelles, and to-date the effect of such barriers on the measurement of absolute diffusion coefficients via MP-FRAP has been neglected.

In the limit that these barriers become extremely close, their impact is relatively straightforward to model because they simply change the dimensionality of the system. For example, it has been shown that an MP-FRAP experiment in microvilli (an extremely narrow tube) can be modeled by one-dimensional diffusion [15, 16]. However, there has been no analysis of boundaries to diffusion positioned at intermediate distances, i.e., neither approaching zero nor at infinity, in order to determine their effects on the reported diffusion coefficient. In this work we will explore the effects of different barrier geometries on the diffusion coefficient reported by MP-FRAP, discuss the mechanism by which these barriers affect the reported diffusion coefficient, and determine the appropriate distances at which the effects of barriers can be neglected. To do this we will simulate the diffusive spread of a distribution of bleached molecules in the presence of various barriers to diffusion via Monte Carlo simulation, then calculate the resultant (two-photon) fluorescence signal, producing an artificial fluorescence *versus* time curve. We will then fit many such curves to the classical MP-FRAP equation, which assumes all barriers are at infinity, and explore how the presence of differing barriers produces errors in the reported diffusion coefficient. In the case of both a single and parallel infinite plane boundaries oriented parallel to the optical axis, we will introduce new models of MP-FRAP that explicitly account for the presence of the boundary/boundaries and explore how these new models improve the accuracy of the reported diffusion coefficients.

II.   MONTE CARLO MODEL OF MP-FRAP

A.   Initial fluorophore distribution

The initial concentration distribution of unbleached fluorophore immediately after the photobleaching pulse, in the limit that the boundaries to diffusion are at infinity, is given by Brown et. al [1]:

$$c(x, y, z; t = 0) = c_o exp \left[-(1/b) q_b \delta_b \langle I_{bl}^b(x, y, z) \rangle \Delta t \right], \quad (1)$$

3

where c_o is the initial equilibrium concentration of fluorophore, b is the number of photons absorbed per photobleaching event, q_b is the quantum efficiency for b-photon photobleaching, δ_b is the multiphoton fluorescence action cross-section of the fluorophore for the order of excitation required for photobleaching, $\langle I_{bl}^b(x, y, z) \rangle$ is the time average of the bleach intensity raised to the bth power, and Δt is the duration of the bleaching pulse.

The bleach intensity can be approximated as a 3D Gaussian [1]:

$$\langle I_{bl}^b(x, y, z) \rangle = \langle I_{bl}^b(0, 0, 0) \rangle exp \left[-\frac{2b(x^2 + y^2)}{\omega_r^2} - \frac{2bz^2}{\omega_z^2} \right], \tag{2}$$

where ω_r and ω_z are the $1/e^2$ radial and axial dimensions of the two-photon focal volume, respectively, and $\langle I_{bl}^b(0, 0, 0) \rangle$ is the time average of the intensity at the two-photon focal volume center raised to the bth power.

For the purpose of simulation, it is more efficient and effective to follow the bleached fluorophores [17–19]. Substituting Eq. 2 into Eq. 1, setting $b = 2$ for a two-photon bleaching process and $c_o = 1$ in anticipation of populating nodes later to determine the amplitude, and noting that the bleach depth parameter is defined as $\beta \equiv (1/b)q_b\delta_b\langle I_{bl}^b(0, 0, 0) \rangle \Delta t$, we find the initial distribution of *bleached* fluorophore:

$$c_{bl}(x, y, z; t = 0) = 1 - exp\left\{ -\beta exp\left[-\frac{4(x^2 + y^2)}{\omega_r^2} - \frac{4z^2}{\omega_z^2} \right] \right\}. \tag{3}$$

The bleach depth parameter was chosen to be $\beta = 0.25$, a value typical of experimental MP-FRAP recovery curves [1, 14]. The axial and radial extents of the focal volume were defined as $\omega_r \equiv 2.6\lambda/(2\pi\text{NA})$ and $\omega_z \equiv 8.8n\lambda/(2\pi(\text{NA})^2)$, respectively, where λ is the wavelength of the excitation laser, n is the index of refraction of the immersion medium, and NA is the numerical aperture of the lens [20]. Our simulations represent the NA extremes of typical water-immersion lenses ($\lambda = 780$ nm, n = 1.33, NA = 0.5 or 1.2). Space was discretized into a regular lattice with spacing defined by the expected diffusion properties (see below). One thousand bleached fluorophores were placed at lattice points using Eq. 3 as the probability distribution, and with the caveat that no fluorophores were allowed outside any diffusive barriers introduced into the system. Multiple occupancy on a single node was permitted.

4

B. Diffusion

Diffusion was modeled as a random walk on a three-dimensional lattice [18, 19, 21, 22]. Lattice spacing was determined by the three-dimensional diffusion equation, $\langle r^2 \rangle = 6Dt$, where the diffusion coefficient, D, was chosen *a priori* and the time step, t, was chosen to be approximately $1/1000$ of the typical diffusive recovery time for a system with a diffusion coefficient D and with radial and axial focal volume widths ω_r and ω_z. For both the low- and high-NA case, D was chosen as $10\mu\mathrm{m}^2/\mathrm{s}$, approximately the experimental diffusion coefficient for 2000 kD fluorescein dextran [14]. The corresponding time steps were chosen as 3.12 μs and 0.376 μs, respectively, and the lattice spacing was calculated to be 13.7 nm and 4.75 nm, respectively.

C. Boundary conditions

Four boundary models were applied to the diffusing system: a single infinite-plane boundary parallel and perpendicular to the optical axis, two infinite parallel-plane boundaries parallel and perpendicular to the optical axis, a hollow infinite-cylinder boundary parallel and perpendicular to the optical axis, and a hollow spherical boundary. In the context of our simulations a barrier is considered infinite if a particle cannot cross the barrier at any time during the simulation. The parallel, cylindrical and spherical boundaries were positioned symmetrically about the focal volume center, and the positions of all of the boundaries were defined as fractions of ω_r or ω_z relative to the focal volume center. All boundaries were assumed to be perfectly reflecting, i.e., any particle attempting to cross a boundary was returned to the node it was occupying when the step began. There were no bleached or unbleached molecules beyond the boundaries at $t = 0$, or at any subsequent point.

D. MP-FRAP

The fluorescence intensity generated by a weak monitoring beam through an m-photon process is given by:

$$F(t) = \frac{\delta_m E}{m} \int \langle I_{mo}^m(x,y,z) \rangle c(x,y,z;t) dxdydz, \tag{4}$$

where δ_m is the multiphoton fluorescence action cross-section of the fluorophore for the order of excitation required to produce fluorescence, E is the collective efficiency of the detection system, and m is the number of photons absorbed per excitation event.

We can calculate the fluorescence that would be generated by the bleached fluorophores were they *not* bleached by re-expressing the integral as a sum over all bleached fluorophore locations (x_i, y_i, z_i). We can also let $(1/m)E\delta_m \to 1$, as it will be divided out when the fluorescence is normalized for fitting:

$$F_{bl}(t) = \sum_i exp\left[-\frac{2b(x_i^2 + y_i^2)}{\omega_r^2} - \frac{2bz_i^2}{\omega_z^2}\right]. \tag{5}$$

To obtain the fluorescence of the *unbleached* molecules, we first normalize the "fluorescence" of the bleached molecules by the pre-bleach fluorescence, F_o, and then subtract from one: $F(t)/F_o = 1 - F_{bl}(t)/F_o$. F_o was determined by first setting $t = 0$ and $\beta = 0.25$ in Eq. 6, below, truncating the sum to the first ten terms, and solving for $F(0)/F_o$. This value was then substituted into $F(0)/F_o = 1 - F_{bl}(0)/F_o$ to deduce F_o from $F_{bl}(0)$.

The natural variation of a Monte Carlo simulated random walk introduced a small amount of noise into the resulting F(t) recovery curves. On top of this, we added Poisson distributed noise to mimic the typical distribution of noise arising from photon counting experiments, and in an amount typical of *in vitro* MP-FRAP experiments [1, 14]. Fluorescence recoveries were terminated when the change in the recovered fluorescence was less than 1% over a time equivalent to the half-time for complete recovery of a freely diffusing system with diffusion coefficient D.

Unless otherwise stated, all simulated F(t) curves were fit to the accepted diffusive recovery model [1]:

$$\frac{F(t)}{F_o} = \sum_{n=0}^{\infty} \frac{(-\beta)^n}{n!} \frac{1}{(1 + n + 2nt/\tau_D)} \frac{1}{(1 + n + 2nt/R\tau_D)^{1/2}}, \tag{6}$$

where τ_D is the characteristic diffusion time and R is the square of the ratio of the axial and radial dimensions of the focal volume. The diffusion coefficient is given by $D = \omega_r^2/8\tau_D$.

III. RESULTS AND DISCUSSION

A. Single plane boundary

We begin our Monte Carlo investigation by introducing a single infinite-plane reflective boundary parallel to the optical axis, at a range of distances measured in units of ω_r relative to the focal volume center. This models diffusion measurements adjacent to cell walls [23–25]. We then generate an initial distribution of bleached molecules according to Eq. 1, with the caveat that no molecules are located beyond the boundary. Then we simulate the random diffusion of those molecules and produce an $F(t)$ curve as described above. The resultant curve is fit to Eq. 6, the MP-FRAP formula that assumes all boundaries are at infinity. The fit (possibly erroneous) diffusion coefficient is then divided by the true diffusion coefficient (defined *a priori* in setting up the diffusion random walk), hence errors due to the presence of a boundary are readily identified by a deviation of this ratio from one. Note that we ceased our simulations at a boundary location of $-0.5\omega_r$ because at this point the average fluorescence from the focal volume in steady state is $< 10\%$ of the value of the unobstructed focal volume.

The resultant data is presented in Fig. 1, and shows that MP-FRAP begins to yield diffusion coefficients significantly different from the input diffusion coefficient (defined hereafter as when the mean fit diffusion coefficient is more than one standard deviation different from the input diffusion coefficient) when the boundary passes a distance of $1.3\omega_r$ from the focal volume center for a high NA lens and $1.5\omega_r$ for a low NA lens. In each of these cases, the fit diffusion coefficient, D, becomes significantly different from the input coefficient before the boundary crosses the focal volume center $(0\omega_r)$, and the deviation is biphasic, with an initial underestimation of the diffusion coefficient becoming an overestimation as the boundary crosses the focal volume center. The underestimation of D is most pronounced when the boundary is in the range of $\sim 0 - 1.5\omega_r$, and we hypothesized that this occurs because the boundary hinders the complete escape of bleached molecules from the focal volume, forcing a selection of fluorophores to reside longer in the neighborhood of the focal volume, thereby lengthening the recovery time. We further hypothesized that as a growing portion of the focal volume becomes "hidden" behind the boundary its characteristic radial size will become smaller than ω_r and fitting of the resultant recovery curves to Eq. 6, which assumes
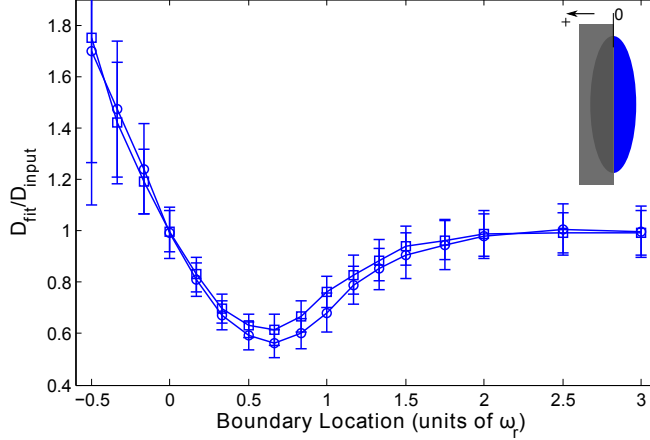
7

FIG. 1. Single boundary parallel the optical axis at a range of positions, presented as fractions of ω_r from the focal volume center, for both a high NA (squares) and low NA (circles) lens. Negative position values indicate that the boundary has crossed the focal volume center (i.e., more than half the focal volume is hidden beyond the boundary). Fluorescence recovery curves were generated via Monte Carlo simulation and fit to the standard MP-FRAP model Eq. 6. Fit diffusion coefficients were normalized to the input diffusion coefficient, hence an accurate fit produces a ratio of one.

that ω_r is the relevant radial length scale, will produce the growing overestimation of D that becomes apparent as the wall approaches $-0.5\omega_r$.

To test these hypotheses we first repeated the series of Monte Carlo simulations, now using a "destructive" boundary instead of a "reflective" one, such that each bleached molecule that attempted to cross the boundary was removed from the simulation. As shown in Fig. 2, removal of the reflected fluorophores eliminated the initial underestimate in D but retained the later overestimate, suggesting that it is indeed reflection of bleached molecules off of the boundary and back into the focal volume that lengthens the recovery time and leads to the initial underestimate of D. One may note that the curves describing the destructive case begin to upswing while those for the reflective case are still in their initial downturn. At this point in the reflective case the effect on recovery is dominated by the fluorophores reflecting back into the region of the focal center, and only as the boundary crosses the focal center does the effect on shortening ω_r begin to overcome particle deflection and reverse the trend, eventually leading to overestimates of D.

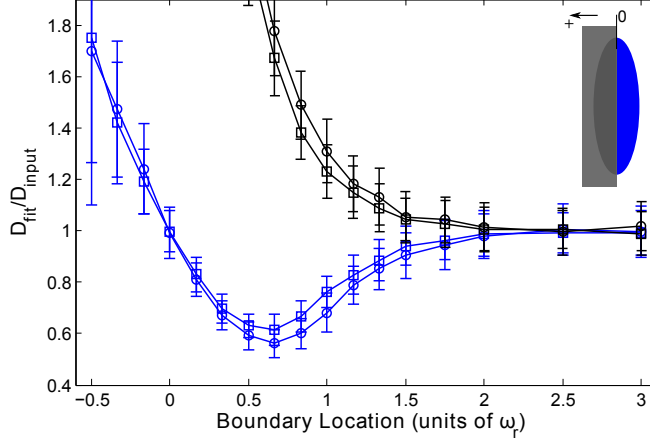Next, to demonstrate the effect that changing the focal volume dimensions has on fluo-

8

FIG. 2. Single "destructive" boundary (black) and "reflective" boundary (blue) parallel to the optical axis at a range of positions, presented as fractions of ω_r from the focal volume center for a high NA (squares) and low NA (circles) lens. Negative position values indicate that the boundary has crossed the focal volume center (i.e., more than half the focal volume is hidden beyond the boundary). Fluorescence recovery curves were generated via Monte Carlo simulation and fit to the standard MP-FRAP model. Fit diffusion coefficients were normalized to the input diffusion coefficient, hence an accurate fit produces a ratio of one.

rescence recovery and fitting, we generated data assuming an unobstructed focal volume and free diffusion, but with ω_r reduced to mimic the influence of the barriers reducing the focal volume as introduced in the previous simulations. We then fit the resulting fluorescence curves assuming a focal volume with the original ω_r. As ω_r was reduced to successively smaller values, the fit diffusion coefficient was increasingly overestimated (data not shown). This reproduces the trend seen in Fig. 2 and suggests that the overestimate in D is indeed due solely to a reduction in the bleaching distribution and monitoring volume, and hence an overestimate of their characteristic size during the fitting process.

Inspection of Fig. 1 also reveals that the low NA curve is more affected by the approach of the barrier than is the high NA curve, with a more significant initial underestimate of D. We hypothesized that this is due to the different aspect ratios of the focal volumes ($\omega_z/\omega_r = 3.75$ for the high NA case and $\omega_z/\omega_r = 9$ for the low NA case). The fastest route for diffusive escape from an initial bleached distribution will be along the shortest dimension of the initial distribution, and the higher aspect ratio of the low NA focal volume
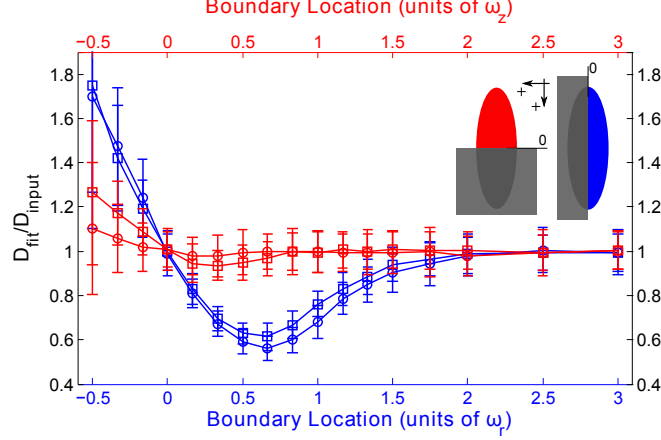
9

FIG. 3. Single boundary parallel (blue) and perpendicular (red) to the optical axis at a range of positions, presented as fractions of ω_r or ω_z, respectively, from the focal volume center for a high NA (squares) and low NA (circles) lens. Negative position values indicate that the boundary has crossed the focal volume center (i.e., more than half the focal volume is hidden beyond the boundary). Fluorescence recovery curves were generated via Monte Carlo simulation and fit to the standard MP-FRAP model. Fit diffusion coefficients were normalized to the input diffusion coefficient, hence an accurate fit produces a ratio of one.

means that the diffusive transport in the direction of the approaching barrier is a more significant contributor to fluorescence recovery for that objective lens than for a higher NA objective, resulting in a more significant effect of the barrier. To test this hypothesis we repeated the series of Monte Carlo simulations, but brought in a barrier to diffusion that was perpendicular to the optical axis. The fastest route for diffusive escape in this geometry is now parallel to the surface of the approaching barrier and thus unhindered by it, leading us to predict that the initial underestimate of D should be greatly reduced. Furthermore, the underestimate of D should now be *least* significant for the low NA case, as that has the highest aspect ratio. As shown in Fig. 3, the initial underestimate of D for the boundary perpendicular to the optical axis is indeed greatly reduced, and is now least significant for the low NA case, thus confirming our hypothesis. Fig. 3 also reveals that MP-FRAP begins to yield diffusion coefficients significantly different from the input diffusion when a boundary perpendicular to the optical axis passes $-0.3\omega_z$ for a high NA lens. For the low NA case, the fit diffusion does not deviate significantly for any of the boundary locations assessed.

To improve the accuracy of the reported diffusion coefficient for the case of a single barrier to diffusion, we have derived an alternative analytical model of the fluorescence recovery (see Appendix) that takes into account the presence of the barrier. For a barrier lying parallel to the optical axis, the new model is:

$$
\frac{F(t)}{F_o'} = \frac{1}{2} \frac{1}{\mathrm{erfc}(-2u/\omega_r)} \sum_{n=0}^{\infty} \frac{(-\beta)^n}{n!} \frac{1}{(n + \mu_n(t))} \frac{1}{(n + \nu_n(t))^{1/2}}
$$
$$
\times \left\{ \mathrm{erfc}\left[-2\left(1 + n/\mu_n(t)\right)^{1/2} \frac{u}{\omega_r}\right] + \exp\left[-\frac{16n}{n + \mu_n(t)} \left(\frac{u}{\omega_r}\right)^2\right] \mathrm{erfc}\left[-2\frac{(1 - n/\mu_n(t))}{(1 + n/\mu_n(t))^{1/2}} \frac{u}{\omega_r}\right]\right\},
$$

$$
(7)
$$

where $\mu_n(t) = 1 + 2nt/\tau_D$, $\nu_n(t) = 1 + 2nt/R\tau_D$, and u is the x or y position of the bleached molecule distribution center relative to the boundary. For a barrier perpendicular to the optical axis, the form is the same but $\mu_n \to \nu_n$ and $\omega_r \to \omega_z$ in the exponential and complementary error functions.

When the new MP-FRAP "single boundary" model is used to fit simulated diffusion curves produced in the presence of a single barrier parallel to the optical axis, the reported diffusion coefficients improve dramatically over a wide range of barrier distances (see Fig. 4). For the case of a barrier perpendicular to the optical axis the reported diffusion coefficients do not improve significantly over the already generally accurate results using the standard model (data not shown). Fig. 4 shows that the fit diffusion coefficient remains accurate until after the boundary has crossed the center of the focal volume ($0\omega_r$), assuming the position of the focal volume with respect to the boundary (u) is known. The fit diffusion coefficient becomes significantly different from the input diffusion coefficient as a boundary parallel to the optical axis passes $-0.15\omega_r$ from the focal volume center for both a high and low NA lens. If the position of the boundary is not known (i.e., beyond the resolution limit of the multi-photon laser scanning microscope), we can allow u to be a free fitting parameter. However, doing so yields erroneous values for the diffusion coefficient for sub-resolution barrier positions (data not shown).

From these simulations we have determined that when an MP-FRAP experiment is performed adjacent to a single plane barrier to diffusion, and the fluorescence recovery curves are fit to the standard MP-FRAP model, erroneous diffusion coefficients can be produced which trend from underestimates of D to overestimates of D as the barrier approaches and passes the center of the focal volume. This is caused by a hindrance of the ability of bleached
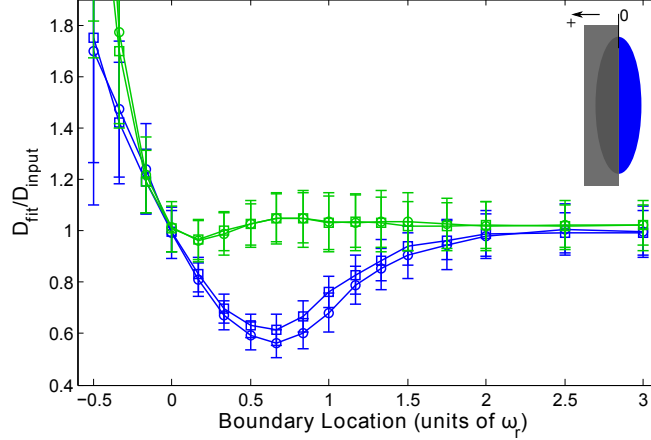
11

FIG. 4. Single boundary parallel to the optical axis at a range of positions, presented as fractions of ω_r from the focal volume center for a high NA (squares) and low NA (circles) lens. Negative position values indicate that the boundary has crossed the focal volume center (i.e., more than half the focal volume is hidden beyond the boundary). Fluorescence recovery curves were generated via Monte Carlo simulation and fit to the standard MP-FRAP model (blue) and the new MP-FRAP model (green) designed for use near a single barrier. Fit diffusion coefficients were normalized to the input diffusion coefficient, hence an accurate fit produces a ratio of one.

molecules to leave the environment of the focal volume, coupled with a truncation of the bleach distribution and monitor volume. Using the standard MP-FRAP model, the onset of these deviations is at a distance of $1.3 - 1.5\omega_r$ for a barrier parallel to the optical axis and $\sim -0.3\omega_z$ for a barrier perpendicular to the optical axis. Due to the high aspect ratio of two-photon focal volumes, the underestimate is most significant when the barrier is parallel to the optical axis. Using the new MP-FRAP single boundary model for a barrier parallel to the optical axis, the initial underestimate is avoided and the point of onset of significant deviations greatly improves to $\sim -0.15\omega_r$.

Most MP-FRAP experiments are performed using a multiphoton laser scanning microscopy (MPLSM) platform, with a radial and axial resolution of imaging of ω_r and ω_z, respectively [26]. Based upon our results, the user can therefore image the spatial distribution of fluorophores and avoid MP-FRAP analysis using the standard model (Eq. 6) where a single barrier parallel to the optical axis is closer than $1.3 - 1.5\omega_r$. For a single barrier perpendicular to the optical axis, the onset of significant errors in the diffusion coefficient is

12

less than the resolution limit of MPLSM, so the conservative user would avoid MP-FRAP analysis when single barriers are closer than ω_z. To improve the range of applicability for a barrier parallel to the optical axis, the user could perform MP-FRAP analysis using the new model (Eq. 7), with which accurate diffusion coefficients can be produced down to the resolution limit, ω_r. The user is then limited in applying MP-FRAP only by the resolution limit of the lens.

B.   Parallel plane boundaries

Two infinite parallel-plane reflective boundaries mimic systems such as the regions between cell walls found in tumor and brain extracellular space [23–25]. To model this system we introduce parallel-plane barriers symmetrically about the focal volume center, positioned parallel or perpendicular to the optical axis at a range of distances measured in units of ω_r or ω_z relative to the focal volume center. As before, the data is presented as D_{fit}/D_{input} as a function of boundary location. In each case, Fig. 5 shows that as the boundaries approach the focal volume, the fit diffusion coefficient begins to drop compared to the input diffusion coefficient. The fit diffusion coefficient becomes significantly different from the input diffusion coefficient as boundaries parallel to the optical axis pass $1.5\omega_r$ from the focal volume center for a high NA lens and $1.8\omega_r$ for a low NA lens. For boundaries perpendicular to the optical axis, the fit diffusion coefficient becomes statistically significantly different from the input diffusion coefficient as the boundaries pass $0.5\omega_z$ from the focal center for a high NA lens. For the low NA case, the fit diffusion does not deviate significantly for any of the boundary locations assessed.

As in the case of the single boundary, the effect on the diffusion coefficient is more significant for the case of two parallel-plane boundaries running parallel to the optical axis. As demonstrated previously, this arises because boundaries parallel to the optical axis reduce the opportunity for diffusing molecules to leave the focal volume via the shorter radial dimension, which predominantly determines the duration of recovery for a freely diffusing sample. This is also shown by the opposite behaviors of low and high NA lenses in the two geometries. When the boundaries are parallel to the optical axis, the low NA lens is the most affected because radial diffusion is more significant in this high aspect ratio focal volume. Conversely, when the boundaries are perpendicular to the optical axis, the low NA lens is
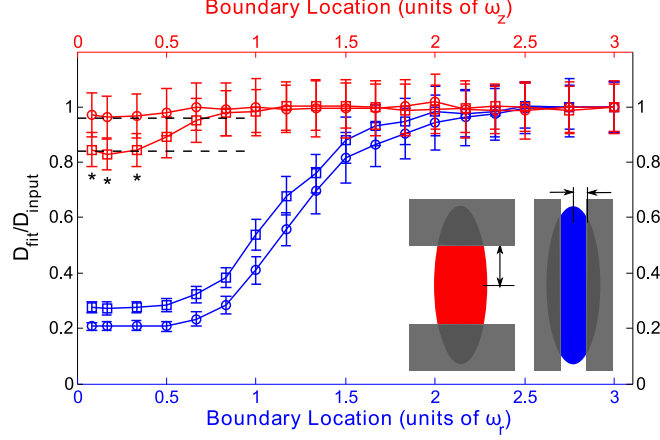
FIG. 5. Two parallel boundaries parallel (blue) or perpendicular (red) to the optical axis at a range of positions symmetric about the focal volume center and presented as fractions of ω_r or ω_z for a high NA (squares) and low NA (circles) lens. Fluorescence recovery curves were generated through Monte Carlo simulation and fit to the standard MP-FRAP model. Fit diffusion coefficients were normalized to the input diffusion coefficient, hence an accurate fit produces a ratio of one. Dashed lines mark the limit of 2D diffusion as indicated by generating data with the 2D MP-FRAP recovery equation and fitting it to the 3D MP-FRAP recovery equation. For data points marked with an asterisk (*), the accurate diffusion coefficient was recovered when the data was fit with the 2D limited MP-FRAP model.

the least affected, for the same reason. Unlike the single boundary case, however, as the boundaries significantly reduce the focal volume, the diffusion coefficient does not rise but levels off. The characteristic length of the focal volume is reduced in the direction normal to the plane surfaces, suggesting that the characteristic recovery time should become shorter, as in the single boundary case. However, as the distance between the planes approaches zero, diffusion is effectively confined to two dimensions, and this effect dominates.

By letting $\omega_z \to \infty$ in Eq. 6 we obtain a two-dimensional form of the MP-FRAP model, valid in the limit of a 2D system perpendicular to the optical axis, and which is identical to the original one-photon FRAP model [3]:

$$\frac{F(t)}{F_o} = \sum_{n=0}^{\infty} \frac{(-\beta)^n}{n!} \frac{1}{1 + n + 2nt/\tau_D}. \tag{8}$$

By generating data using this 2D formula and then fitting the data to the 3D model we find that in the limit of 2D diffusion the 3D model should yield a value of the diffusion coefficient

that is 0.84 ± 0.04 times the accepted value for a high NA lens and 0.96 ± 0.03 times the accepted value for a low NA lens. These limits are plotted in Fig. 5 as the dashed lines and coincide with the values of the normalized diffusion coefficients at small values of ω_z as determined by the Monte Carlo simulations of MP-FRAP. The asterisks(*) mark data sets that, when re-fit with the 2D MP-FRAP model given by Eq. 8, recovered the input diffusion coefficient to within one standard deviation.

To improve the accuracy of the reported diffusion coefficient for the case of parallel infinite-plane barriers to diffusion, we have derived an alternative analytical model of the fluorescence recovery (see Appendix) that takes into account the presence of the barriers. For barriers lying parallel to the optical axis, the new model is:

$$
\frac{F(t)}{F_o''} = \frac{1}{3} \frac{1}{\operatorname{erf}(2u/\omega_r)} \sum_{n=0}^{\infty} \frac{(-\beta)^n}{n!} \frac{1}{(n+\mu_n(t))} \frac{1}{(n+\nu_n(t))^{1/2}} \left\{ \operatorname{erf} \left[-2 \left(1 + n/\mu_n(t)\right)^{1/2} \frac{u}{\omega_r} \right] \right.
$$

$$
\left. + \exp \left[-\frac{16n}{n+\mu_n(t)} \left(\frac{u}{\omega_r} \right)^2 \right] \left(\operatorname{erf} \left[-2 \frac{(1 - n/\mu_n(t))}{(1 + n/\mu_n(t))^{1/2}} \frac{u}{\omega_r} \right] + \operatorname{erf} \left[-2 \frac{(1 + 3n/\mu_n(t))}{(1 + n/\mu_n(t))^{1/2}} \frac{u}{\omega_r} \right] \right) \right\}.
$$
(9)

For barriers perpendicular to the optical axis, the form is the same but $\mu_n \to \nu_n$ and $\omega_r \to \omega_z$ in the exponential and error functions.

When the new MP-FRAP "parallel boundary" model is used to fit simulated diffusion curves produced assuming the presence of parallel-plane barriers parallel to the optical axis, the reported diffusion coefficients improve dramatically over a wide range of barrier distances (see Fig. 6). For the case of a barrier perpendicular to the optical axis the reported diffusion coefficients do not improve significantly over the already widely accurate results using the standard model (data not shown). Fig. 6 shows that the fit diffusion coefficient becomes significantly different from the input diffusion coefficient as boundaries parallel to the optical axis pass ω_r from the focal volume center for both a high and low NA lens. If the position of the boundary is not known (i.e., beyond the resolution limit of the MPLSM), we can allow u to be a free fitting parameter. However, doing so yields poor fits for sub-resolution barrier positions (data not shown).

From these simulations we have determined that when an MP-FRAP experiment is performed between parallel-plane barriers to diffusion, erroneous diffusion coefficients can be produced that underestimate D. This is caused by a hindrance of the ability of bleached molecules to leave the environment of the focal volume, coupled with an approach of the
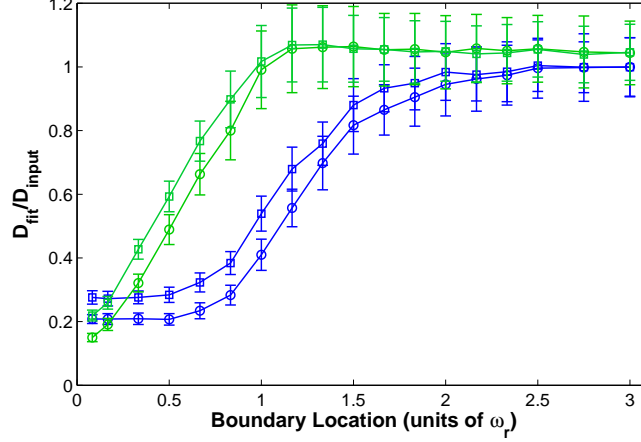
FIG. 6. Two parallel plane boundaries parallel to the optical axis at a range of positions, presented as fractions of ω_r from the focal volume center for a high NA (squares) and low NA (circles) lens. Fluorescence recovery curves were generated via Monte Carlo simulation and fit to the standard MP-FRAP model (blue) and the new MP-FRAP model (green) designed for use near a single barrier. Fit diffusion coefficients were normalized to the input diffusion coefficient, hence an accurate fit produces a ratio of one.

system to a two-dimensional geometry. The onset of these deviations is at a distance of $1.5 - 1.8\omega_r$ for barriers parallel to the optical axis, and < 0.1 to $\sim 0.5\omega_z$ for barriers perpendicular to the optical axis. Due to the high aspect ratio of two-photon focal volumes, the underestimate is most significant when the barriers are parallel to the optical axis. Based upon our results, the user can therefore image the spatial distribution of fluorophores and avoid MP-FRAP analysis using the standard model (Eq. 6) where barriers parallel to the optical axis are closer than $1.5 - 1.8\omega_r$ for high and low NA lenses, respectively. For barriers perpendicular to the optical axis, the onset of significant errors in the diffusion coefficient is less than the resolution limit of MPLSM, so the conservative user would avoid MP-FRAP analysis when single barriers are closer than ω_z. To improve the range of applicability for barriers parallel to the optical axis, the user could perform MP-FRAP analysis using the new model (Eq. 9) enabling accurate diffusion coefficients to be produced down to the resolution limit, ω_r. The user is then limited in applying MP-FRAP only by the resolution limit of the lens.

C. Cylindrical boundary

An infinite hollow cylindrical boundary provides an excellent approximation for neuronal dendrites and axons, in which transport measurements are of interest in neurobiological research [27, 28]. In our simulations we introduce a cylindrical boundary both parallel and perpendicular to the optical axis, positioned symmetrically about the focal volume center at a range of distances measured in units of ω_r and ω_z. Again, the data is presented as D_{fit}/D_{input} as a function of boundary location. As with the case of the parallel-plane boundaries, Fig. 7 shows that as the boundaries approach the focal volume, the fit diffusion coefficient begins to drop compared to the input diffusion coefficient, and these effects occur at larger values of ω_r for the case of a cylindrical boundary parallel to the optical axis than for corresponding values of ω_z in the perpendicular case. Specifically, the diffusion coefficient becomes significantly lower than the input diffusion coefficient as the radius of a cylinder parallel to the optical axis becomes smaller than $1.8\omega_r$ for a high NA lens and $2\omega_r$ for a low NA lens. The diffusion coefficient becomes statistically significantly lower than the input diffusion coefficient as the radius of a cylinder perpendicular to the optical axis becomes smaller than $0.7\omega_z$ for a high NA lens and $0.3\omega_z$ for a low NA lens.

Similar to the parallel plane boundaries, we find that when the cylindrical boundary is sufficiently constricting the diffusion effectively becomes one dimensional. Consequently, although the size of the available volume decreases there is no overestimate in the apparent D after the initial underestimate. In the limit of 1D diffusion, the MP-FRAP model can be altered to account for the dimensional change. By letting $\omega_r \to \infty$ in Eq. 6 we obtain a 1D form of the MP-FRAP model for diffusion along the optical axis:

$$\frac{F(t)}{F_o} = \sum_{n=0}^{\infty} \frac{(-\beta)^n}{n!} \frac{1}{(1 + n + 2nt/R\tau_D)^{1/2}}. \tag{10}$$

By generating data using this 1D model and fitting it to the 3D model we find that in the limit of 1D diffusion the 3D model should yield a value of the diffusion coefficient that is 0.026 ± 0.001 times the accepted value for a high NA lens and 0.006 ± 0.001 times the accepted value for a low NA lens. These limits are plotted in Fig. 7 as the dashed lines and coincide with the values of the normalized diffusion coefficients at small values of ω_r as determined by the Monte Carlo simulations of MP-FRAP. The asterisks(*) mark data sets that, when re-fit with the 1D standard MP-FRAP model, recovered the input diffusion
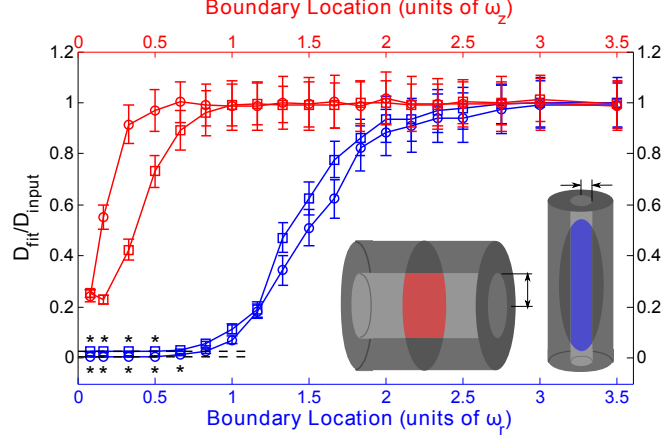
17

FIG. 7. Cylindrical boundary parallel (blue) and perpendicular (red) to the optical axis at a range of positions, symmetric about the focal volume center and presented as fractions of ω_r or ω_z, for a high NA (squares) and low NA (circles) lens. Fluorescence recovery curves were generated through Monte Carlo simulation and fit to the standard MP-FRAP model. Fit diffusion coefficients were normalized to the input diffusion coefficient, hence an accurate fit produces a ratio of one. Dashed lines mark the limit of 1D diffusion as indicated by generating data with the 1D MP-FRAP recovery equation and fitting it to the 3D MP-FRAP recovery equation. For data points marked with an asterisk (*), the accurate diffusion coefficient was recovered when the data was fit with the 1D limited MP-FRAP model.

coefficient, within one standard deviation.

From these simulations we have determined that when an MP-FRAP experiment is performed within an infinite cylindrical barrier to diffusion, erroneous diffusion coefficients can be produced that underestimate D. This is caused by a hindrance of the ability of bleached molecules to leave the environment of the focal volume, coupled with an approach of the system to a one-dimensional geometry. The onset of these deviations is at a radius of $\sim 1.8-2\omega_r$ for a cylinder parallel to the optical axis, and $\sim 0.3 - 0.7\omega_z$ for a cylinder perpendicular to the optical axis. Due to the high aspect ratio of two-photon focal volumes, the underestimate is most significant when the cylindrical barrier is parallel to the optical axis. Based upon our results, the user can therefore image the spatial distribution of fluorophores and avoid MP-FRAP where the cylinder parallel to the optical axis has a radius smaller than $\sim 1.8\omega_r$. A cylinder perpendicular to the optical axis rests in the image plane, and can be
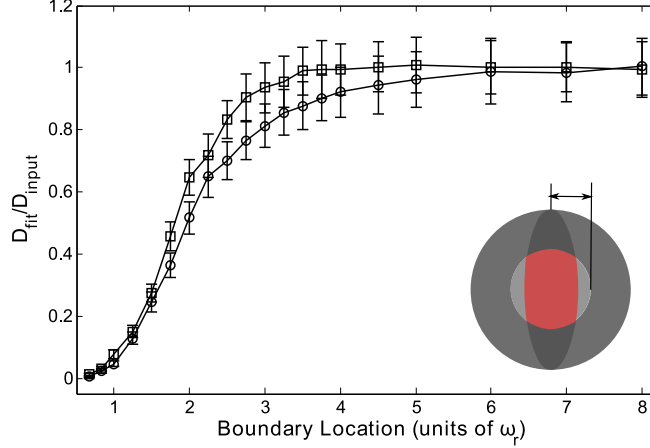
FIG. 8. Spherical boundary at a range of positions, symmetric about the focal volume center and presented as fractions of ω_r, for a high NA (squares) and low NA (circles) lens. Fluorescence recovery curves were generated through Monte Carlo simulation and fit to the standard MP-FRAP model. Fit diffusion coefficients were normalized to the input diffusion coefficient, hence an accurate fit produces a ratio of one.

imaged with the superior ω_r radial resolution of imaging. Hence the radius of the cylinder can be readily determined down to a resolution significantly smaller than ω_z and the user would avoid cylinders that have a radius smaller than $\sim 0.7\omega_z$.

D. Spherical boundary

A hollow spherical boundary well approximates a cell body, cell nucleus or dendritic spine [29–31]. We introduce the spherical boundary symmetrically about the focal volume center at a range of distances measured in units of ω_r. The data is presented as D_{fit}/D_{input} as a function of boundary location. Fig. 8 shows that the fit diffusion coefficient drops rapidly relative to the input diffusion coefficient as the boundaries narrow in on the focal volume. Specifically, the diffusion coefficient becomes significantly lower than the input diffusion coefficient as the radius of the sphere becomes smaller than $2.75\omega_r$ for a high NA lens and $3.75\omega_r$ for a low NA lens.

As the sphere becomes sufficiently small, many (and eventually all) of the bleached molecules will be unable to leave the focal volume. This suggests that the standard 3D MP-FRAP model (Eq. 6), which assumes free diffusion of the entire fluorophore population,

19

may be inappropriate to fit the recovery. The concept of an "immobile fraction" has been discussed previously [1, 32] in the context of fluorophore populations attached to the extracellular matrix or cell cytoskeleton, and involves an additional fitting parameter to account for the incomplete recovery caused by a subset of immobile fluorophores. We refit the data generated for free diffusion within a spherical boundary using standard 3D MP-FRAP with a fitting parameter for an immobile fraction, but did not achieve significantly more accurate values for the diffusion coefficient (data not shown). This arises because the case of an immobile fluorophore population and our case of a trapped but mobile population are only superficially similar. In the case of an immobile fraction, a subset of fluorophores are permanently (relative to the duration of the experiment) fixed in space. The remaining fluorophores, however, are assumed to diffuse freely. In the case of fluorophores confined within a spherical boundary, however, while many fluorophores remain within the focal volume they are always free to move. As the bleached molecules spread from their initial center-heavy distribution to a more uniform distribution, the fluorescence of the sample changes. The shape of the recovery is subtly, yet significantly different from the case of immobile fluorophores, and fitting with this added parameter does not significantly improve the resultant diffusion coefficient.

From these simulations we have determined that when an MP-FRAP experiment is performed within a spherical barrier to diffusion, erroneous diffusion coefficients can be produced which underestimate D. This is caused by a hindrance of the ability of bleached molecules to leave the environment of the focal volume. The onset of these deviations is at a radius of $\sim 2.75 - 3.75\omega_r$ and is not improved by fitting with an immobile fraction term. This radius is significantly greater than the ω_r resolution of imaging of MPLSM systems. Therefore, based upon our results, the user can image the spatial distribution of fluorophores and avoid MP-FRAP within spherical compartments where the sphere has a radius smaller than $\sim 3.75\omega_r$.

IV. CONCLUSION

In this paper, we have used Monte Carlo simulations to model multiphoton fluorescence recovery after photobleaching in the presence of reflecting boundaries of various geometries and sizes. Our results show that MP-FRAP can produce erroneous values of the diffusion

coefficient even when the boundaries are significantly larger than the focal volume. The size limit at which the boundaries begin affecting the MP-FRAP measurement varies with the geometry of the boundary, with the two extremes being a single plane perpendicular to the optical axis (D becomes erroneous at $\sim -0.3\omega_z$) and a sphere (D becomes erroneous at $3.75\omega_r$). The significance of the error is a function of the aspect ratio of the focal volume (i.e., the NA) and the orientation of the barriers, with barriers to diffusion in the radial direction having the greatest effect. Using our guidelines, a researcher can first image a sample using two-photon fluorescence, then measure and locate a region with the appropriate dimensions to allow an accurate measurement of the diffusion coefficient using the appropriate model. For both a single and paired barriers parallel to the optical axis, we present a new model of MP-FRAP that can be used to produce accurate diffusion coefficients for boundary distances much closer than is possible with the standard MP-FRAP model. Measurements of diffusion via MP-FRAP can now be completed with confidence in an array of *in vivo* systems previously believed to be inaccessible.

Appendix

The time-dependent concentration distribution of unbleached fluorophore following the bleach pulse is given by Brown et. al. [1]. When written in Cartesian coordinates for a concentration distribution centered at the origin, the expression is:

$$c(x,y,z;t) = c_o \sum_{n=0}^{\infty} \frac{(-\beta)^n}{n!} \frac{1}{\mu_n(t)\nu_n(t)^{1/2}} \exp\left[-\frac{2bn}{\omega_r^2}\frac{x^2}{\mu_n(t)}\right] \exp\left[-\frac{2bn}{\omega_r^2}\frac{y^2}{\mu_n(t)}\right] \exp\left[-\frac{2bn}{\omega_z^2}\frac{z^2}{\nu_n(t)}\right],$$
$$(A.1)$$

where

$$\mu_n(t) = 1 + 8bnDt/\omega_r^2, \tag{A.2}$$

$$\nu_n(t) = 1 + 8bnDt/\omega_z^2. \tag{A.3}$$

For the case of a single infinite plane boundary at the origin we can develop an approximate analytical model by replacing the barrier with the real distribution and an "image" distribution placed symmetrically about the origin at a positions u and $-u$, which represent the distance of the real distribution from the barrier (see Fig. 9). In the region to the right of the origin, this closely models the behavior of the system: as the distributions spread due to
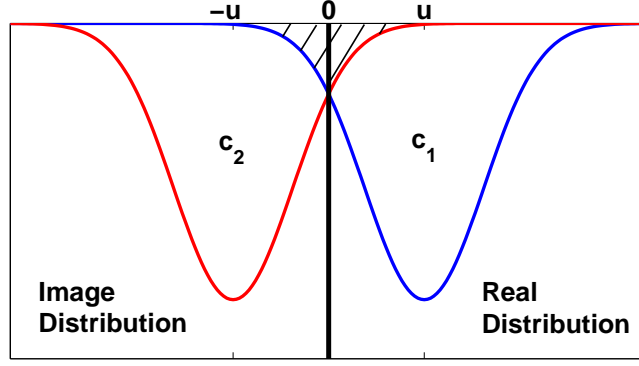
FIG. 9. Placement of real and "image" bleached molecule concentration distributions for the case of a single infinite plane boundary. The overlap of the image distribution in the region of the real distribution as the two distributions spread ($t > 0$) mimics the behavior of diffusing molecules that bounce off the barrier and back into the focal volume. At $t = 0$, there will be overcounting of bleached molecules when the two distributions are close to the barrier. This error will remain small until the image distribution peak approaches the barrier.

diffusion, the overlap of the image distribution with the real distribution mimics the behavior of those fluorophores that bounce off the barrier and back into the space to the right of the barrier. With this approximation, there is some over counting of the initial fluorophore population (hatched region in Fig. 9) when the two distributions are oriented close to the barrier. This "extra" distribution of bleached molecules will evolve over time, producing an error in the fluorescence as a function of time, and hence in the diffusion coefficient, D. However, this error remains small until the peak of the image distribution approaches the origin. As the two distributions perfectly overlap the error in D disappears, then grows again as the distribution centers continue past one another. The combined concentration distribution, assuming a barrier parallel to the optical axis in the x-dimension, is given by

$$c'(x, y, z; t) = (1/2)[c_1(x - u, y, z; t) + c_2(x + u, y, z; t)], \qquad (A.4)$$

where c_1 and c_2 are produced by introducing a coordinate shift into Eq. A.1, and the 1/2 accounts for the fact that we have introduced an image distribution that doubles the true concentration of fluorophore.

The fluorescence recovery is monitored by a low-intensity laser beam centered on the real

concentration distribution, and is given by

$$F'(t) = \frac{\delta_m E}{2m} \int \langle I_{mo}^m(x-u,y,z) \rangle \, c'(x,y,z;t) dxdydz, \tag{A.5}$$

where δ_m is the multiphoton fluorescence action cross section, E is the collection efficiency of the system, m is the number of photons required to produce fluorescence from a single fluorophore, and $\langle I_{mo}^m(x-u,y,z) \rangle$ is the time-average of the bleach intensity raised to the mth power, given by

$$\langle I_{mo}^m(x-u,y,z) \rangle = \langle I_{mo}^m(0,0,0) \rangle \, e^{-(2m/\omega_r^2)(x-u)^2} e^{-(2m/\omega_r^2)y^2} e^{-(2m/\omega_z^2)z^2}. \tag{A.6}$$

It is important to note that while for the standard model derivation the integral in $F(t)$ is taken over all space, in the presence of a single barrier the integral along the dimension interrupted by the barrier (in this case x) is taken only from $0 \to \infty$.

When Eqs. A.4 and A.6 are substituted into Eq. A.5 and the integral is performed, the simplified expression for the fluorescence recovery, letting $m = b = 2$ is:

$$\frac{F'(t)}{F_o'} = \frac{1}{2} \frac{1}{\mathrm{erfc}(-2u/\omega_r)} \sum_{n=0}^{\infty} \frac{(-\beta)^n}{n!} \frac{1}{(n+\mu_n(t))} \frac{1}{(n+\nu_n(t))^{1/2}}$$

$$\times \left\{ \mathrm{erfc}\left[-2\left(1+n/\mu_n(t)\right)^{1/2} \frac{u}{\omega_r} \right] + \exp\left[-\frac{16n}{n+\mu_n(t)} \left(\frac{u}{\omega_r}\right)^2 \right] \mathrm{erfc}\left[-2\frac{(1-n/\mu_n(t))}{(1+n/\mu_n(t))^{1/2}} \frac{u}{\omega_r} \right] \right\}, \tag{A.7}$$

where F_o' is the equilibrium value of the fluorescence before the photobleaching pulse. We can compare Eq. A.7 with the standard MP-FRAP model (Eq. 6) to gain some insight into the new form. As noted earlier, the $1/2$ arises from our introduction of the image distribution. The first complementary error function comes from the calculation of F_o', which is evaluated over the limits $0 \to \infty$. The first part of the summation, appearing on the first line, is the standard MP-FRAP equation. Finally, the contribution to the fluorescence recovery is shared between the real concentration distribution, represented by the second complementary error function, and the image concentration distribution, represented by the exponential $\times$ complementary error function term. In the limit $u \to \infty$,

$$\frac{F'(t)}{F_o'} = \frac{1}{2} + \frac{1}{2} \sum_{n=0}^{\infty} \frac{(-\beta)^n}{n!} \frac{1}{(n+\mu_n(t))} \frac{1}{(n+\nu_n(t))^{1/2}}. \tag{A.8}$$

With the image distribution center pushed to negative infinity, the distribution of unbleached molecules in the region of the focal volume (at positive infinity) is at equilibrium, and

23

contributes a constant $1/2$ to the normalized fluorescence. Meanwhile, the real distribution center translates to infinity with the focal volume, and produces a fluorescence recovery with the same form as a standard fluorescence recovery. At full recovery $(t \to \infty)$, $F'(t)/F'_o = 1$, as expected.

This derivation can be repeated for a wall perpendicular to the optical axis by introducing the appropriate coordinate shifts in z, rather than x or y. The result has the same form as Eq. A.7, but with $\omega_r \to \omega_z$ and $\mu_n(t) \to \nu_n(t)$ in the exponential and complimentary error functions.

Following similar logic leading to the derivation of the "one boundary" MP-FRAP model, we can also produce an approximate analytical model for use in the presence of two parallel infinite-plane boundaries. In this case, we place the real concentration distribution at the origin, and model two boundaries placed symmetrically about the distribution center (at u and $-u$) with an image distribution on the opposite side of each barrier (at $-2u$ and $2u$). The concentration distribution for this configuration has three parts, $c''(x, y, z; t) = (1/3)[c_1(x - 2u, y, z, ; t) + c_2(x, y, z; t) + c_3(x + 2u, y, z; t)]$, and the integration to determine the fluorescence is limited to $-u \to u$ along the dimension in which the barriers appear. The resulting normalized fluorescence recovery, for boundaries parallel to the optical axis, is given by:

$$\frac{F''(t)}{F''_o} = \frac{1}{3} \frac{1}{\mathrm{erf}(2u/\omega_r)} \sum_{n=0}^{\infty} \frac{(-\beta)^n}{n!} \frac{1}{(n + \mu_n(t))} \frac{1}{(n + \nu_n(t))^{1/2}} \left\{ \mathrm{erf}\left[-2\left(1 + n/\mu_n(t)\right)^{1/2} \frac{u}{\omega_r} \right] \right.$$

$$+ \exp\left[-\frac{16n}{n + \mu_n(t)} \left(\frac{u}{\omega_r} \right)^2 \right] \left(\mathrm{erf}\left[-2\frac{(1 - n/\mu_n(t))}{(1 + n/\mu_n(t))^{1/2}} \frac{u}{\omega_r} \right] + \mathrm{erf}\left[-2\frac{(1 + 3n/\mu_n(t))}{(1 + n/\mu_n(t))^{1/2}} \frac{u}{\omega_r} \right] \right) \right\}.$$

$$(A.9)$$

Similar to the single boundary formula, the $1/3$ arises from the introduction of the two image distributions. The first error function comes from the calculation of F''_o, which is evaluated from $-u \to u$. The standard MP-FRAP model appears again, and is weighted by contributions from the real distribution, represented by the second error function, and the image distributions, represented by the two exponential $\times$ error function terms. In the limit $u \to \infty$,

$$\frac{F''(t)}{F''_o} = \frac{2}{3} + \frac{1}{3} \sum_{n=0}^{\infty} \frac{(-\beta)^n}{n!} \frac{1}{(n + \mu_n(t))} \frac{1}{(n + \nu_n(t))^{1/2}}. \qquad (A.10)$$

Here, the image distributions contribute a constant $1/3$ each to the normalized fluores-

cence, while the real distribution recovers as would a standard MP-FRAP curve. At full recovery $(t \to \infty)$, $F(t)''/F_o'' = 1$, as expected.

As with the one boundary model, this derivation can be repeated for walls perpendicular to the optical axis by introducing the appropriate coordinate shifts in z, rather than x or y. The result has the same form as Eq. A.9, but with $\omega_r \to \omega_z$ and $\mu_n(t) \to \nu_n(t)$ in the exponential and error functions.

ACKNOWLEDGMENTS

[1] E. B. Brown, E. S. Wu, W. Zipfel, and W. W. Webb, Biophys. J., **77**, 2837 (1999).

[2] W. Denk, J. H. Strickler, and W. W. Webb, Science, **248**, 73 (1990).

[3] D. Axelrod, D. E. Koppel, J. Schlessinger, E. Elson, and W. W. Webb, Biophys. J., **16**, 1055 (1976).

[4] M. Edidin, M. Zagyansky, and T. Lardner, Science, **191**, 466 (1976).

[5] D. E. Koppel, D. Axelrod, J. Schlessinger, E. L. Elson, and W. W. Webb, Biophys. J., **16**, 1315 (1976).

[6] D. A. Berk, F. Yuan, M. Leunig, and R. K. Jain, Biophys. J., **65**, 2428 (1993).

[7] D. Magde, E. L. Elson, and W. W. Webb, Biopolymers, **13**, 29 (1974).

[8] H. Qian, M. P. Sheetz, and E. L. Elson, Biophys. J., **60**, 910 (1991).

[9] K. M. Berland, P. T. C. So, and E. Gratton, Biophys. J., **68**, 694 (1995).

[10] J. Mertz, C. Xu, and W. W. Webb, Opt. Lett., **20**, 2532 (1995).

[11] W. Watanabe, S. Matsunaga, T. Higashi, K. Fukui, and K. Itoh, J. Biomed. Opt., **13**, 031213 (2008).

[12] R. M. Williams, W. R. Zipfel, M. L. Tinsley, and C. E. Farnum, Biophys. J., **93**, 1039 (2007).

[13] S. Basu, V. Rodionov, M. Terasaki, and P. J. Campagnola, Opt. Lett., **30**, 159 (2005).

[14] K. D. Sullivan, W. H. Sipprell III, E. B. Brown Jr., and E. B. Brown III, Biophys. J., **96**, 5082 (2009).

[15] S. Coscoy, F. Waharte, A. Gautreau, M. Martin, D. Louvard, P. Mangeat, M. Arpin, and F. Amblard, Proc. Natl. Acad. Sci. USA, **99**, 12813 (2002).

[16] F. Waharte, C. M. Brown, S. Coscoy, E. Coudrier, and F. Amblard, Biophys. J., **88**, 1467 (2005).

[17] D. M. Soumpasis, Biophys. J., **41**, 95 (1983).

[18] F. P. Coelho, W. L. Vaz, and E. Melo, Biophys. J., **72**, 1501 (1997).

[19] M. J. Saxton, Biophys. J., **81**, 2226 (2001).

[20] E. Brown and W. Webb, "Caged compounds. methods of enzymology series v. 291," (Academic Press, 1998) Chap. Two-Photon Activation of Caged Calcium with Submicron, Submillisecond Resolution, pp. 356–380.

[21] P. K. Tsourkas, M. L. Longo, and S. Raychaudhuri, Biophys. J., **95**, 1118 (2008).

[22] S. Wieser, M. Axmann, and G. J. Schütz, Biophys. J., **95**, 5988 (2008).

[23] G. Alexandrakis, E. B. Brown, R. T. Tong, T. D. McKee, R. B. Campbell, Y. Boucher, and R. K. Jain, Nat. Med., **10**, 203 (2004).

[24] D. K. Binder, M. C. Papadopoulos, P. M. Haggie, and A. S. Verkman, J. Neurosci., **24**, 8049 (2004).

[25] M. C. Papadopoulos, J. K. Kim, and A. S. Verkman, Biophys. J., **89**, 3660 (2005).

[26] W. R. Zipfel, R. M. Williams, and W. W. Webb, Nat. Biotechnol., **21**, 1369 (2003).

[27] M. Gabso, E. Neher, and M. E. Spira, Neuron, **18**, 473 (1997).

[28] H. Schmidt, O. Arendt, E. B. Brown, B. Schwaller, and J. Eilers, J. Neurochem., **100**, 727 (2007).

[29] K. Svoboda, D. W. Tank, and W. Denk, Science, **272**, 716 (1996).

[30] A. Majewska, E. Brown, J. Ross, and R. Yuste, J. Neurosci., **20**, 1722 (2000).

[31] K. Holthoff, D. Tsay, and R. Yuste, Neuron, **33**, 425 (2002).

[32] T. J. Feder, I. Brust-Mascher, J. P. Slattery, B. Baird, and W. W. Webb, Biophys. J., **70**, 2767 (1996).